




Article

Optimal Design of an Interior Permanent Magnet Synchronous Motor with Cobalt Iron Core

Pedro P. C. Bhagubai , Luís F. D. Bucho, João F. P. Fernandes *  and P. J. Costa Branco 

IDMEC, Instituto Superior Técnico, University of Lisboa, 1049-001 Lisboa, Portugal; pedro.bhagubai@tecnico.ulisboa.pt (P.P.C.B.); luis.bucho@tecnico.ulisboa.pt (L.F.D.B.); pbranco@tecnico.ulisboa.pt (P.J.C.B.)

* Correspondence: joao.f.p.fernandes@tecnico.ulisboa.pt

Abstract: The use of a cobalt-iron (VaCoFe) core is investigated as an alternative to silicon-iron (FeSi) in the design of interior permanent magnet synchronous motors (IPMSM). Considering VaCoFe and FeSi cores, a spoke-type IPMSM geometry is optimized for a torque range up to 40 N·m, providing a general comparative analysis between materials. This is done considering the application of a four-motor competition vehicle's powertrain. A genetic optimization algorithm is coupled to the motor's electromagnetic and thermal hybrid analytical/finite-element model to provide sufficiently accurate results within a feasible time. VaCoFe allows an estimated increase of up to 64% in torque for the same efficiency level, or up to 5% in efficiency for the same torque. After optimization and using a detailed time-dependent model, a potential 3.2% increase in efficiency, a core weight reduction of 4.1%, and a decrease of 9.6% in the motor's core volume were found for the VaCoFe at 20 N·m. In addition, for the same motor volume, the VaCoFe allows an increase of 51.9% in torque with an increase of 1.1% in efficiency when compared with FeSi.

Keywords: electric vehicle applications; electromagnetic model; optimization; thermal model; vanadium cobalt



Citation: Bhagubai, P.P.C.; Bucho, L.F.D.; Fernandes, J.F.P.; Costa Branco, P.J. Optimal Design of an Interior Permanent Magnet Synchronous Motor with Cobalt Iron Core. *Energies* **2022**, *15*, 2882. <https://doi.org/10.3390/en15082882>

Academic Editor: Federico Barrero

Received: 7 March 2022

Accepted: 10 April 2022

Published: 14 April 2022

Publisher's Note: MDPI stays neutral with regard to jurisdictional claims in published maps and institutional affiliations.



Copyright: © 2022 by the authors. Licensee MDPI, Basel, Switzerland. This article is an open access article distributed under the terms and conditions of the Creative Commons Attribution (CC BY) license (<https://creativecommons.org/licenses/by/4.0/>).

1. Introduction

The continuous electrification of the transportation system is an important step to achieving the required high-standard target emissions. However, to achieve higher levels of electrification, new, increasingly demanding specifications have been arising for electrical traction systems. While the levels of efficiency are already very high in electrical machines, their current specific power (power-to-weight and power-to-volume) is still limited. This is a key challenge for mobility and transportation systems where, typically, there is limited space and energy storage. This is a particularly important issue in the development of all-electric aircrafts, where the required target of 9–13 kW/kg still remains to be achieved [1].

Therefore, the increase in the specific power of electrical machines is still today a current challenge among the industrial and research communities. To address this challenge, two current approaches are being followed: (a) using new electromagnetic materials to expand their current electromagnetic and thermal limits and (b) using optimization techniques to further optimize their geometry.

Regarding the new electromagnetic materials, the Vanadium-Cobalt-Iron (VaCoFe) alloy has been emerging as a potential candidate to increase the current specific power of electrical machines. This alloy presents a high saturation point (2.2–2.4 T) [2]. However, associated with this higher saturation point, higher core losses may occur, making it unclear whether the increase of specific power is achieved with high efficiency. Furthermore, higher core losses may prevent the full use of VaCoFe's high magnetic flux density due to thermal limits. Several studies have identified the VaCoFe as a potential candidate to increase the specific power of synchronous reluctance machines [3–5] and permanent magnet synchronous machines [6,7] for high-speed and aerospace applications. In electric

car traction applications, few have successfully applied VaCoFe comparatively to FeSi. However, some reports state a 20% increase of specific-torque/power when using VaCoFe alloys [8,9]. Furthermore, an important target in aircraft applications is increasing the current limits of electrical machines (around 5 kW/kg) to values of 9–13 kW/kg for future electric aircraft applications [10]. In [6], the use of VaCoFe has shown the possibility of increasing specific power up to 10 kW/kg and increasing the efficiency by about 3% in aircraft applications.

In [11], a high-performance spoke-type IPMSM to be integrated into a four-motor vehicle powertrain has been designed with an FeSi core. The designed motor was built and validated through experimental tests. To improve the performance of this vehicle, VaCoFe is considered a promising material, and, as such, questions arise on quantifying the influence of the core material on machine design and performance. A spoke-type IPMSM geometry is optimized considering FeSi and VaCoFe cores for a range of torque/efficiency to provide a general comparative analysis between materials for the application. The non-dominated sorting genetic algorithm II (NSGA-II) [12] is used over a hybrid analytical/finite-element (FE) model of the motor, similar to the method validated before [11]. This kind of electrical machine design based on optimization tools using hybrid analytical/FE models is a successful method [13] that also takes less computation time than purely FE models [14] while providing good results. It allows large-scale design optimization to achieve high-power density designs of permanent magnet-based machines such as IPMSM [15] and other topologies, including novel axial flux PMSM [16]. Particularly in [15], large-scale multi-objective optimization using a differential evolution algorithm with a FE model was applied to obtain an optimal spoke-type IPMSM design for a Formula E competition (110 N·m at 6000 rpm), experimentally validated, achieving 12.2 N·m/kg. Additionally, obtaining optimal designs allows a comparative analysis between motor characteristics, such as winding configuration or cooling system, as was completed in [17] for a 300 N·m, 1800 rpm IPMSM machine. In this work, the focus is on the core lamination material.

Our presented motor model provides sufficiently accurate electromagnetic and thermal results and can be computed within a feasible time in the context of the optimization process. It consists of a stationary time 2D FE model used to calculate the motor's flux distribution, in conjunction with analytical expressions to estimate losses in the core and permanent magnets and the operating temperature. From these, the parameters of the IPMSM equivalent circuit are computed, and torque and efficiency values are obtained. Each core material is characterized by its B-H and power loss density constitutive curves. Because the optimization results are highly dependent on the accuracy of the model, experimental BH and specific loss curves are obtained for a test magnetic circuit of VaCoFe laminations.

Based on this model, we show in this work that VaCoFe core results in higher torque and efficiency across the considered ranges, with an estimated increase of up to 5% in efficiency for the same torque or up to 64% torque increase for the same efficiency level. However, because the density of VaCoFe is higher than FeSi, and because it is possible to have larger PMs and slots in VaCoFe designs, there is a less pronounced difference in weight for the overlapping torque range. Because VaCoFe laminations are around three times more expensive than FeSi due to their material cost and post-processing requirements to achieve optimal properties [2], whether the difference in specific torque and the increase in efficiency achieved with VaCoFe concerning FeSi cores is considerable enough to justify these increased costs has to be subject to further application-specific cost/benefit analysis.

This work follows the preliminary work developed in [18] by including new experimental tests on the VaCoFe alloy and its impact on optimization. A more detailed analysis of the optimized solutions, using a time-dependent FE approach, is carried out to obtain accurate results for torque ripple, harmonics, and losses. A four-motor competition electric vehicle's powertrain, with 80 N·m at 8000 rpm, is here considered as a case study.

2. Electric Motor Materials

The impact of different magnetic core materials on the IPMSM's performance was studied, in particular, FeSi and VaCoFe. The IPMSM modeling and optimization were characterized by their respective B-H and specific losses curves. These characteristic curves were estimated for VaCoFe from experimental testing on a sample magnetic circuit. The test circuit, presented in Figure 1, was made of two 'E'-type lamination stacks, with two windings (1:1 ratio between primary and secondary) around the central leg.

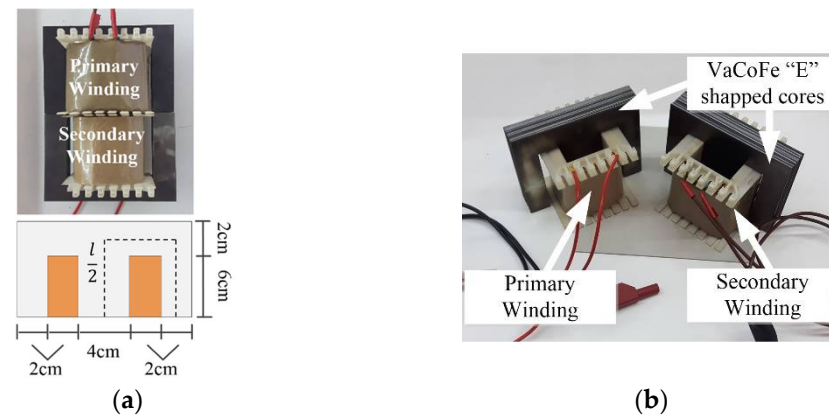


Figure 1. Magnetic circuit used in the experimental tests made from VaCoFe. (a) Magnetic circuit dimensions with half of the average path, l , (dashed line), and (b) core and windings' identification.

To obtain these curves, sinusoidal voltage waveforms were applied to the primary winding. For each frequency value, f , a high enough voltage to saturate the circuit was applied, and measurements were taken for subsequently decreasing values, as described in [19]. For each applied voltage, the current in the primary winding, i_1 , and induced voltage in the secondary winding, u_2 , were measured. These allow estimating the peak magnetic field intensity, H , and flux density, B , by applying Ampère's and Faraday's laws, given by Equations (1) and (2). The resulting VaCoFe B-H curve is presented in Figure 2. The loss density for several frequency values was computed from the power in the magnetic circuit, considering the induced voltage in the secondary, u_2 , to avoid the influence of the losses in the primary winding, Equation (3). In Equations (1)–(3), $|\overline{U}_2|$ is the rectified mean value of the voltage induced in the secondary winding, N the number of turns, A the cross-section area of the circuit's central leg, I_1 the maximum current on the primary winding, m the weight of the circuit's core, and T the period of the waveforms. Because of the symmetry of the circuit and the central leg being twice the width of the lateral legs, the length l is that of the average path along one side of the circuit (double the length of the dashed line in Figure 1).

$$B = \frac{|\overline{U}_2|}{4fNA} \quad (1)$$

$$H = \frac{NI_1}{l} \quad (2)$$

$$p = \frac{1}{m} \left(\frac{1}{T} \int_0^T i_1(t)u_2(t)dt \right) \quad (3)$$

The specific losses curve is presented for a frequency of 400 Hz, which is the nominal frequency of the machine, and, additionally, for 50 Hz as reference. This material's properties have been shown to be sensitive to the manufacturing process; however, if an appropriate cutting technique followed by a heat treatment process is applied to the laminations, it is possible to limit the negative impact and reach values up to 2.4 T [2]. The tested circuit's laminations were treated according to the manufacturer's specifications, and as such, specific losses are close to the expected properties presented in the datasheet for both frequencies, Figure 3. However, there is still a more noticeable deviation around the

knee-point for the BH curve results, as according to the manufacturer's datasheet, VaCoFe laminations are expected to reach around 2.0 T at the B-H curve's knee-point. The curves obtained experimentally were considered in the optimization process to take into account the sensitivity of the material to the manufacturing processes.

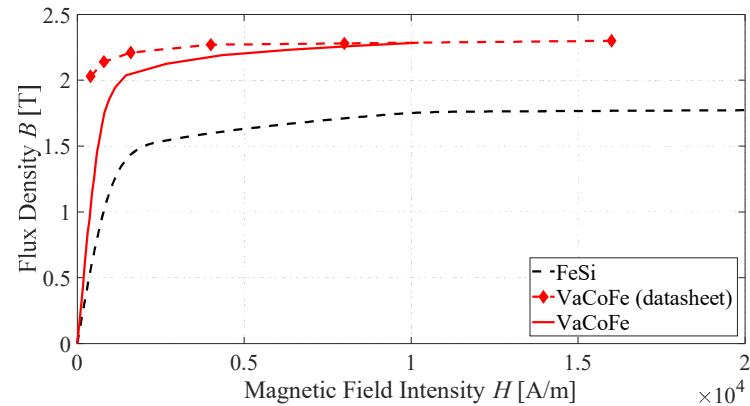


Figure 2. B-H curve of lamination materials: FeSi, VaCoFe obtained experimentally and from manufacturer's datasheet.

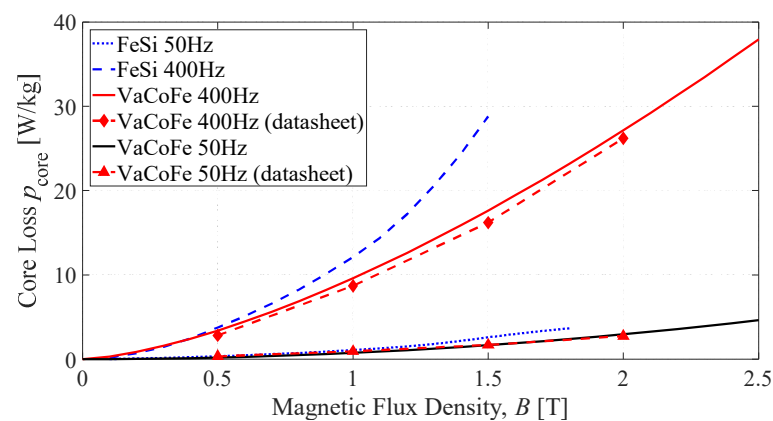


Figure 3. Specific losses curve of lamination materials: FeSi, VaCoFe obtained experimentally and from manufacturer's datasheet, at 50 Hz and 400 Hz.

A high-performance, low losses FeSi alloy for electrical machines is considered, with a BH curve knee-point around 1.5 T. It has been characterized for optimization previously in [11] with the prototyping of a 20 kW FeSi PMSM, from which the results are presented, for comparison, in Figures 2 and 3. It is noted that FeSi presents a density of 7650 kg/m³ and VaCoFe a density of 8120 kg/m³.

For both cases, NH40 grade Neodymium-Boron (NdFeB) permanent magnets with remnant magnetic flux $B_r = 1.2$ T and a maximum temperature rating of 120 °C are considered. The shaft is made of stainless steel, a non-magnetic material.

3. Spoke-Type Interior Permanent Magnet Synchronous Machine Model

The presented model considers the electromagnetic and thermal aspects of the IPMSM and is based on an FE model used to compute lumped parameters. This type of model is chosen for computationally intensive optimizations because it provides a compromise between computation time and accuracy [14]. To maintain a low computation time, the geometry of the core was simplified, and only a pole pair of the machine was modeled. A stationary time 2D FE model was used to calculate the motor's flux distribution and, in conjunction with analytical expressions, operating temperatures, efficiency, and torque were estimated.

This methodology was used for the multi-objective optimization of the machine. After optimization, the final solutions were simulated using a time-dependent study. The proposed model was validated experimentally for a similar geometry of IPMSM, with the FeSi core considered in Figure 2. This FeSi IPMSM was previously developed and experimentally tested in [11]. In this previous work, the same electromagnetic-mechanical models were used (2D FE model + analytical models) to simulate an IPMSM with FeSi for a 4-motor competition electric vehicle's powertrain that was required to develop a total maximum of 80 N·m at 8000 rpm to achieve the desired performance. An example of a competition track with an optimized lap is presented in Figure 4, along with the total torque profile in Figure 5. After simulation and verification of the fulfillment of the requirements, a final solution of the machine was built and tested. After some mechanical adjustments to the rotor to facilitate the cutting of the laminated silicon iron, it had a rated torque and efficiency of 18.2 N·m and 90.0%, respectively. The machine was built and tested (Figure 6), and the efficiency map was obtained from experimental tests, as shown in Figure 7.

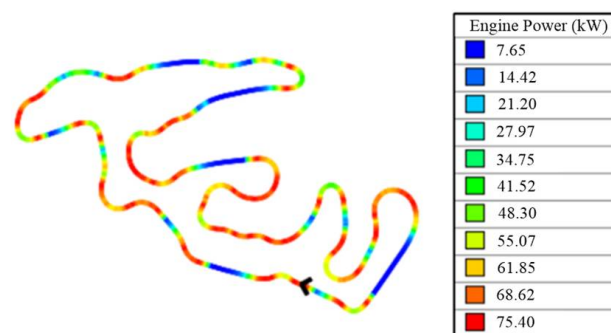


Figure 4. FSAE Autocross Germany track simulation.

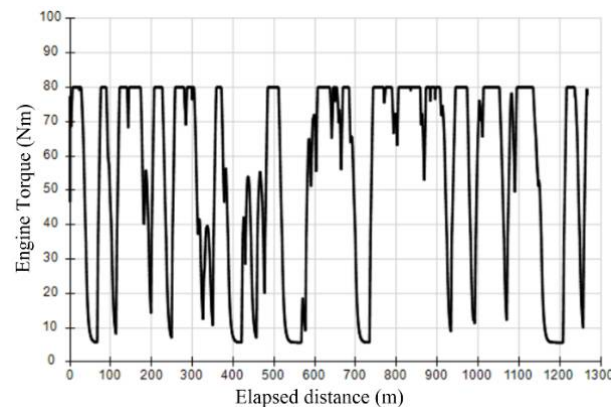


Figure 5. Instantaneous motor's torque along the track.

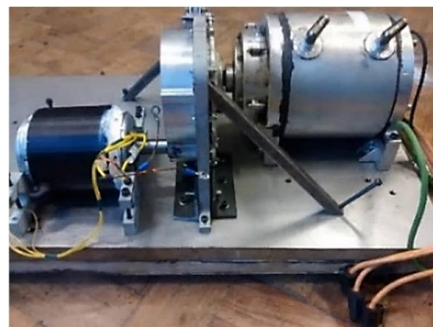


Figure 6. 20 kW IPMSM with FeSi core in experimental setup [11].

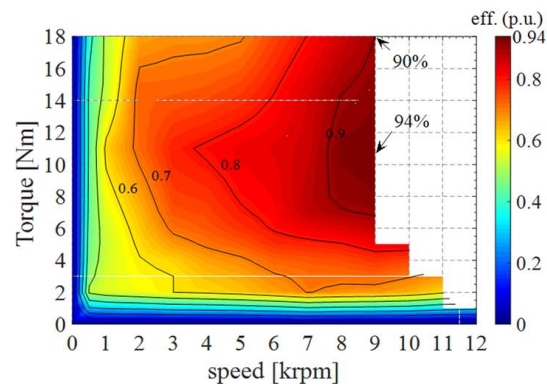


Figure 7. Torque-efficiency map obtained experimentally [11].

Following the previous work, a new IPMSM with VaCoFe was optimized and compared with the results of an optimized FeSi machine. This was intended to evaluate the potential of extending the limits of the IPMSM using VaCoFe alloys.

3.1. Geometry and Winding Layout

The base geometry of the IPMSM to be optimized using FeSi and VaCoFe is presented in Figure 8, along with the variable dimension parameters that will be taken as decision variables. It is a 24-slot stator and an 8-pole rotor, with the following variable dimension parameters: rotor radius, r_r , shaft radius, r_s , permanent magnet width, w_m , and length, l_m , the stator tooth width, w_t and length, l_t , outer ring width, w_s , and the airgap size, g .

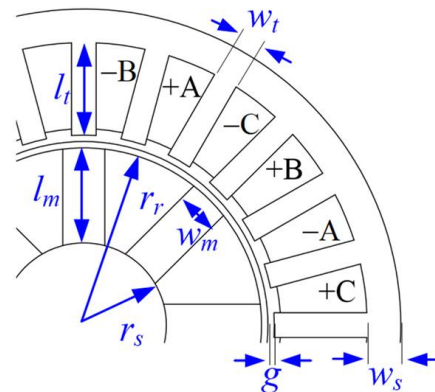


Figure 8. Interior permanent magnet synchronous machine model geometry for optimization, defined by the presented dimensions (labeled in blue) and winding layout (labeled in black).

These variable dimension parameters were decision variables in the optimization process to maximize the IPMSM's torque and efficiency, constrained within the ranges presented in Table 1. These ranges were set according to the available mounting space in the competition car. Because there are four identical motors mounted in each wheel's suspension, the outer dimensions were limited. The maximum outer radius and length were equal to 50 mm and 80 mm, respectively. Each combination of decision variables represents different geometries that are then iteratively compared against each other in terms of torque and efficiency following the multi-objective genetic algorithm process.

The slot/pole combination was chosen according to the nominal rotation speed required for the competition vehicle. In the stator, a single-layer concentrated winding layout (with phase sequence A, $-C$, B, $-A$, C, $-B$) was adopted to maximize the fundamental component of the airgap magnetomotive force wave and to simplify the manufacturing process (Figure 8).

Table 1. Optimization decision variables.

Variable	Description	Range
r_r	Rotor radius	20–40 mm
w_s	Stator outer ring width	1–20 mm
w_m	Magnet width	1–15 mm
l_m	Magnet length	5–20 mm
w_t	Teeth width	1–10 mm
l_t	Teeth length	7–20 mm
g	Airgap size	1–1.5 mm
r_s	Shaft radius	5–30 mm
J_{oq}	Torque producing current density (q axis)	5–80 A/mm ²

3.2. Electromagnetic Model

The optimization, being an iterative process, requires a high number of simulations, which can result in a very high computational burden. To reduce the computational optimization time to a more feasible one, a hybrid analytical/finite element (FE) model was used to represent the IPMSM. This allows taking the nonlinearity of the core materials into consideration without resorting to a more computationally-consuming full FE time-dependent model. The analytical model was based on the synchronous d - q reference frame IPMSM’s equivalent circuit, considering iron losses through an equivalent core-loss resistance, Figure 9. To obtain the machine’s equivalent circuit parameters, a 2D stationary FE model was used. Using the FE model, the magnetic flux linkages, the machine’s d - q inductances, L_d and L_q , and the equivalent core-loss resistance, R_c , were estimated.



Figure 9. Synchronous machine equivalent circuit considering core-losses on a d - q reference frame.

The steady-state torque is the sum of two contributions: electromagnetic, T_{EM} , and reluctance torque, T_{Rel} , and is given by Equation (4), where n_{pp} is the number of pole pairs, Ψ_{PM} is the permanent magnet linked flux and i_{od} , i_{oq} are the torque generating currents. In Figure 9, v_d , v_q , i_d , i_q are the d - q axis stator voltages and currents, i_{od} , i_{oq} are the torque generating currents, R_s is the phase winding resistance, R_c is the equivalent core-loss resistance, L_d and L_q are the d - q inductances, ω_M is the rotor angular speed, and Ψ_{PM} the permanent magnet linked flux which, for the considered machine topology, is aligned with the d -axis.

$$T = T_{EM} + T_{Rel} = \frac{3}{2} n_{pp} (\Psi_{PM} i_{oq} + (L_d - L_q) i_{od} i_{oq}) \tag{4}$$

The electromagnetic component of the generated torque was chosen to be optimized as it provides a good indication of the total torque of the machine and simplifies the machine’s model equations, thus reducing its computational time. With $i_{od} = 0$, one obtains Equations (5)–(7), which decreases the number of FE simulations required, as the computation of L_d is no longer required.

$$T = T_{EM} = \frac{3}{2} n_{pp} \Psi_{PM} i_{oq} \tag{5}$$

$$i_d = -\frac{\omega_M L_q i_{oq}}{R_c} \tag{6}$$

$$i_q = i_{oq} + \frac{\omega_M \Psi_{PM}}{R_c} \tag{7}$$

Losses estimation in the magnetic core and permanent magnets are traditionally made from resource-intensive time-dependent FE simulations for a certain rotation speed to include the effect of harmonics [20,21]. Therefore, to obtain an estimation in less computational time, analytical expressions for the locked-rotor case considering only the magnetic flux fundamental component are employed [22]. For a sinusoidal source, the main sources of magnetic flux density time harmonics in the machine core are the mmf wave, determined by the choice of winding layout and the nonlinearity of the core material's BH curve. On the other hand, for the present analysis, only one type of layout is considered, and core saturation constraints are set according to each of the considered core materials; Table 2. This limits the harmonic content of the magnetic flux in the core and, as such, for optimization purposes, this estimation of iron losses considering only the fundamental component is appropriate. A more accurate loss model is applied later, in Section 6, to some selected optimized motor designs to further refine the obtained solutions. The overall efficiency estimated with both models presented a deviation under 0.3%, which is within an acceptable margin for a proposed prototype design at this stage.

Table 2. Optimization constraints by type and respective ranges.

Constraint	Range
Geometrical	
Weight	<5 kg
Stator outer radius	<50 mm
Motor stack length	=80 mm
Thermal	
PM's temperature	<120 °C
Windings' temperature	<180 °C
Magnetic	
Magnetic flux density	FeSi: <1.6 T VaCoFe: <2.2 T

With these considerations, the core loss density was estimated with Steinmetz coefficients, obtained from the experimental results presented in Figures 2 and 3. Considering a sinusoidal variation of the flux density in the rotor and stator cores, core loss density, p_{core} , is given by Equation (8), where f is the frequency of the flux density and B_m its amplitude, the Steinmetz coefficients k_h , k_e and k_{exc} , determined for each core material (VaCoFe and FeSi). The amplitude of flux density, B_m , was obtained from the stationary FE model, with the stator flux aligned with d and q rotor axes.

$$p_{core} = k_h f B_m^2 + k_e (f B_m)^2 + k_{exc} (f B_m)^{1.5} \quad (8)$$

Despite the relatively high stator frequency, because of the radial orientation of the permanent magnets ($l_m > w_m$), only the top section, nearer to the airgap, is subject to induced currents. To avoid time-dependent simulations but still retain a possible estimation, loss density in the permanent magnets, p_{PM} , was estimated from Equation (9), which is an analytical approximation valid for parallelepiped shape magnets not considering skin effect [23]. In Equation (9), ρ_{PM} , d_{PM} , and l_{PM} are resistivity, depth, and length of the permanent magnet, respectively. Despite not considering the skin effect, the locked-rotor loss in the permanent magnets, as a worst case, is a majorant of the loss during machine operation at the tested nominal speed. Therefore, it provides a majorant of the permanent magnet losses, and the optimization algorithm minimizes them by favoring advantageous dimensions. Further analysis in Section 6 shows that, at the nominal operation point, losses in the permanent magnets were much lower than losses in the windings and the core, so the impact of its estimation on the accuracy of the computation of the PMSM's efficiency was further reduced. Additionally, these losses could be minimized for the final design by

segmenting the magnets and limiting induced current paths [23]; however, for optimization, the magnets' length is taken as the stack length (80 mm).

$$p_{PM} = \frac{(\pi f B_m)^2}{8\rho_{PM}} \left(\frac{d_{PM}^2 l_{PM}^2}{d_{PM}^2 + l_{PM}^2} \right) \tag{9}$$

After the computation of the core and permanent magnets loss densities, the equivalent resistance R_c can be computed with Equation (10), where V_{core} and V_{PM} are the rotor plus stator core volume and permanent magnets volume, respectively.

$$R_c = \frac{3}{2} \frac{(\omega_M(L_d i_{od} + \Psi_{PM}))^2 + (\omega_M L_q i_{oq})^2}{p_{core} V_{core} + p_{PM} V_{PM}} \tag{10}$$

3.3. Finite Element Model

To reduce the complexity, size, and computation time of the FE model, only one pole pair of the machine was simulated. The machine was cut along flux density distribution symmetry lines where continuity conditions are imposed on the external boundaries, Figure 10. Each domain was defined with the corresponding materials' properties: copper coils, magnetic core, NdFeB PMs, and stainless-steel shaft.

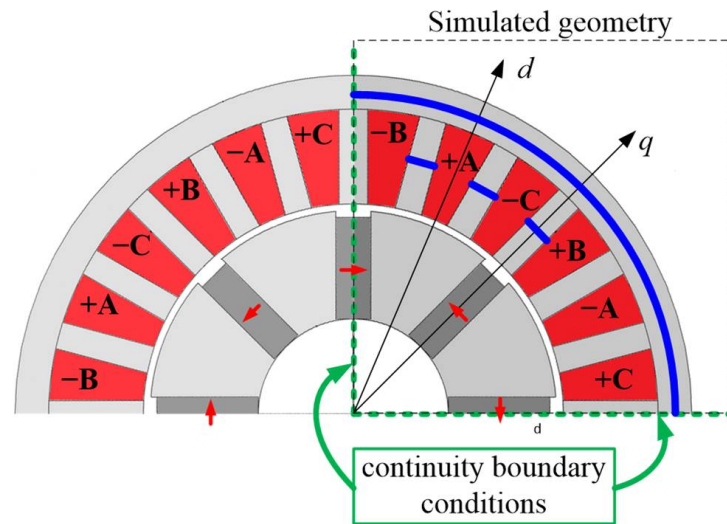


Figure 10. Finite element model of an example geometry representation with the rotor's q-axis aligned with phase A.

According to the presented electromagnetic model, stationary simulations with the rotor aligned with each of the d - q axes were considered. The current in each phase is given by (11) to (13). If the rotor's q ($\theta = 90^\circ$) or d ($\theta = 0^\circ$) axis is aligned with phase A, the Park transformation results in $i_{od} = 0$ and $i_{oq} = I_m$, or $i_{od} = I_m$ and $i_{oq} = 0$, respectively, for each case. By adjusting the rotor's position, d - q linked fluxes Ψ_q and Ψ_d , and B_q and B_d flux density distributions were estimated from the FE results.

$$i_A = I_m \cos(\omega t) \tag{11}$$

$$i_B = I_m \cos(\omega t - 2\pi/3) \tag{12}$$

$$i_C = I_m \cos(\omega t + 2\pi/3) \tag{13}$$

With $i_{od} = 0$, the flux $\Psi_d = 0$, so only Ψ_q and Ψ_{PM} need to be obtained. The flux Ψ_q was obtained as a function of i_{oq} current by aligning the rotor q -axis with the stator in a position of minimum flux linkage with the stator coil (coil A) and without considering permanent magnets flux (making $\Psi_{PM} = 0$). For simplification, cross saturation was neglected, and L_q

was estimated as depending only on i_{oq} (14). The permanent magnet-linked flux, Ψ_{PM} , was obtained by aligning the d -axis with stator coil A without current ($i_{od} = 0$) and measuring the d -axis linked flux.

$$L_q = \frac{\Psi_q}{i_{oq}} \Big|_{i_{od}=0} \quad (14)$$

According to the considered model, the estimation of R_c from the locked-rotor core losses was obtained from the amplitude of flux density B_m in the magnetic core and PMs Equation (15). B_d and B_q were obtained by simulations with the rotor aligned with d and q rotor axes and $\Psi_{PM} \neq 0$.

$$B_m = |B_d - B_q| \quad (15)$$

Flux distribution results were also used to evaluate maximum magnetic flux density constraints on the core. It was evaluated along strategic lines on the magnetic circuit (blue lines in Figure 10) along the stator teeth and back iron. In the rotor, the average flux density was computed, as the non-uniform flux distribution here makes it difficult for it to be characterized by a line. If the maximum flux density value in these lines or the average flux density in the rotor was above a defined threshold, the core was considered to violate the magnetic constraint; Table 2. This method was used to avoid localized peaks of high flux concentration resulting in the rejection of promising geometries during optimization.

3.4. Maximum Operating Temperature Estimation

Thermal phenomena in the machine are critical to determining if a design is viable. The operation temperature in the windings is limited by the insulation between turns. If it is too high, it can degrade and cause short circuit paths that degrade a machine's performance. However, the magnets are the most critical part as their characteristic curves are dependent on their temperature and can be partially or fully demagnetized through heating. According to these limits, the operating temperature must be estimated and constrained below a maximum value for optimization.

A simplified model was used to estimate the maximum operating temperature of the machine during optimization with low computational time. The motor will be required to provide nominal power in short bursts, so the maximum operating steady-state temperature can be estimated for the worst-case scenario to evaluate if the optimized solutions are viable. A water-cooled cooling jacket was considered, previously designed and implemented, that achieves a heat transfer coefficient of $h = 1053 \text{ Wm}^{-2}\text{K}^{-1}$ [11].

The estimation considers convective heat transfer in the airgap and dissipation from the machine surface to the cooling system and environment. Thermal conduction in the rotor and stator core were neglected as the conductive thermal resistance in metallic materials is very low when compared to convective ones. The machine produces heat from Joule losses in the rotor core Equation (8), and PMs Equation (9), which is dissipated through the airgap. This is added to heat from stator core and copper windings' losses Equation (16) and dissipates through the cooling jacket into the environment.

$$P_{Cu} = \frac{3}{2} R_s (i_d^2 + i_q^2) \quad (16)$$

The airgap convective heat transfer coefficient was defined by Equation (17) for heat transfer between concentric rotating cylinders Equations (18) and (19) [24]. The air's thermal conductivity is k , D_h is the hydraulic diameter, Nu the Nusselt number, ν the air's kinematic viscosity, and ω_M the rotor's mechanical rotational speed. For the typical range of this motor's speed and the considered geometrical dimensions, the Taylor's number is $Ta > 10^4$, and so the flow will be turbulent; thus, Nu is given by Equation (18).

$$h_{ag} = \frac{k}{D_h} Nu \quad (17)$$

$$Nu = 0.409 Ta^{0.241} \quad (18)$$

$$Ta = \frac{\omega_M^2 (r_r + g) \left(\frac{D_h}{2}\right)^3}{\nu^2}, \quad D_h = \frac{2\left(\pi\left((r_r + g)^2 - r_r^2\right)\right)}{\pi\left((r_r + g) - r_r\right)} \quad (19)$$

The convection thermal resistances of the airgap, R_{ag} , and of the path from the machine's outer surface to the environment through the cooling system, R_S , were obtained from Equations (20) and (21). The airgap heat transfer surface is given by $S_{ag} = 2\pi r_r L$, with $S = 2\pi RL$ being the electric machine's surface with outer radius $R = 50$ mm and length $L = 80$ mm. The heat transfer was described by the thermal equation system Equation (22), where T_s and T_{amb} are the surface and ambient temperatures.

$$R_{ag} = \frac{1}{h_{ag} S_{ag}} \quad (20)$$

$$R_S = \frac{1}{hS} \quad (21)$$

$$\begin{cases} T_s = R_S(P_{stator} + P_{Cu}) + T_{amb} \\ T_{rotor} = R_{ag}(P_{rotor} + P_{PM}) + T_s \end{cases} \quad (22)$$

4. Optimization

The goals of optimization are to obtain the highest torque and efficiency values, with the machine dimensions subjected to the available space in the vehicle and the thermal and magnetic limitations. The objective functions are then the maximization of the electromagnetic torque and efficiency at 400 Hz, (23), given by (24) and (25), respectively. To perform the machine's optimization, the multi-objective genetic algorithm NSGA-II [12] was applied, with the evaluation of the objective functions and constraints taken from the FE and analytical models' results. The NSGA-II is resilient to local optimal points, making it suitable for finding the global minimum/maximum of the solution space, populating it evenly, which is relevant for the intended comparative analysis. These multi-objective optimizations' results are represented as 2D Pareto front curves (torque vs. efficiency) that allow a general comparative analysis of the impact on machine design of the considered core materials and output power.

$$\max_{x \in \Omega} (f_1(x), f_2(x)) \quad (23)$$

$$f_1 = T_{EM} = \frac{3}{2} n_{pp} \Psi_{PM} i_{oq} \quad (24)$$

$$f_2 = \eta = \frac{T_{EM} \omega_M}{T_{EM} \omega_M + p_{core} V_{core} + \rho_{PM} V_{PM}} \quad (25)$$

Geometrical decision variables, presented and highlighted in Figure 8, will be optimized within the ranges listed in Table 1. In addition to these, the torque-producing current density, J_{oq} , was also taken as a decision variable to account for the direct relation to the resulting torque and temperature constraints. A winding slot filling factor of $f_w = 0.4$ was considered.

The constraints, their classification, and allowed ranges are listed in Table 2. These include constraints derived from application-specific requirements, such as maximum dimensions and weight, but also thermal limitations of windings and permanent magnets and maximum magnetic flux density in the core. The latter was set as 1.6 T for FeSi and 2.2 T for VaCoFe. Objective functions and constraints were evaluated with the presented electromagnetic and thermal models for each element of each generation.

5. Results

Two genetic optimizations were conducted for magnetic core material, FeSi and VaCoFe, for 150 generations of 200 population elements each, sufficient for the solutions to converge within a feasible time (26 h for FeSi and 30 h for VaCoFe). The Pareto front

curves of the last generation are presented in Figures 11 and 12. Across the considered range, VaCoFe core resulted in higher torque and efficiency values. In relation to FeSi cores, VaCoFe is estimated to increase up to 5% in efficiency for the same torque (23 N·m) or increase torque up to 64% for the same efficiency level (93.3%). This increase is due to the relatively flat profile of the obtained efficiency curve being highly dependent on its estimation according to the presented model. The accuracy of the model was validated previously for a 20 kW FeSi PMSM built and tested in [11], and experimentally obtained curves were considered here for the VaCoFe core.

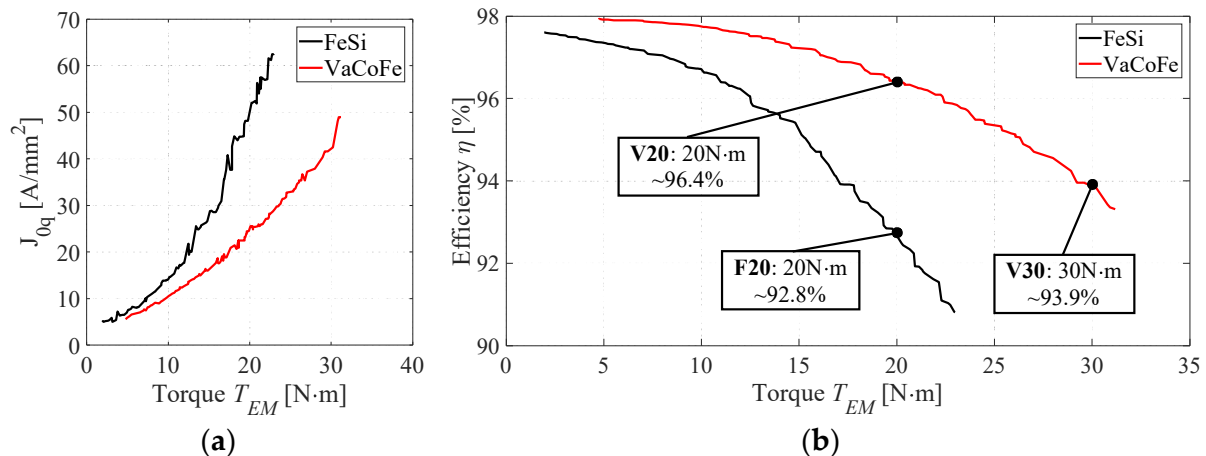


Figure 11. Decision variable for FeSi and VaCoFe core optimization sorted by increasing torque: (a) torque-producing current density J_{0q} and (b) Pareto front with objective function efficiency and electromagnetic torque values of the last generation. Geometries selected for further analysis are represented.

For both materials, permanent magnet dimensions are at the maximum possible values without overlap, maximizing linked flux and torque, Figure 12c,d. Given VaCoFe's higher saturation point, it allows higher magnetic flux and, therefore, wider magnets. The rotor and stator temperatures for the last generation, sorted by increasing torque, are presented in Figure 13. Thermal constraints only limit the machine's performance on the top range torque due to mainly the current density, Figure 11a. As such, the cooling system was well-dimensioned for the considered dimension ranges.

On the other hand, the magnetic constraint is a limiting factor. The magnetic flux densities for both core materials are at constraint level, Figure 14. As such, along the Pareto front, increased current density maximizes torque, decreases efficiency, and machine dimensions vary to keep the magnetic flux density around the maximum allowed value. This resulted in higher FeSi core volumes for the same torque, with VaCoFe core volumes staying approximately constant from 20 N·m upwards, Figure 15a. The latter is possible because of the slight decrease in magnet size, compensated with the current density to achieve these higher torque values at the cost of efficiency.

It is estimated that, for machines with the same torque, the volume of VaCoFe core is, on average, 8.6% less than that of FeSi one. However, because the density of VaCoFe (8120 kg/m³) is higher than FeSi (7650 kg/m³), the difference in core weight is less pronounced at 3.7%, Figure 15b). Considering the weight of copper coils, PMs, and a stainless-steel shaft, VaCoFe machines reached a maximum torque density of 7.2 N·m/kg, while FeSi machines reached 5.4 N·m/kg. These results indicate that it is possible to achieve higher torque densities with VaCoFe and higher nominal torque points.

Total weight is impactful on the competition vehicle application's performance, so the torque density of the motor is a critical factor. The required nominal torque was 20 N·m per motor, so there was a potential 3.6% increase in efficiency with an optimal VaCoFe core design; Figure 11. At this point, the lower copper and PM weight makes up for the heavier VaCoFe core; however, both designs ended up with a total weight of around 4.3 kg.

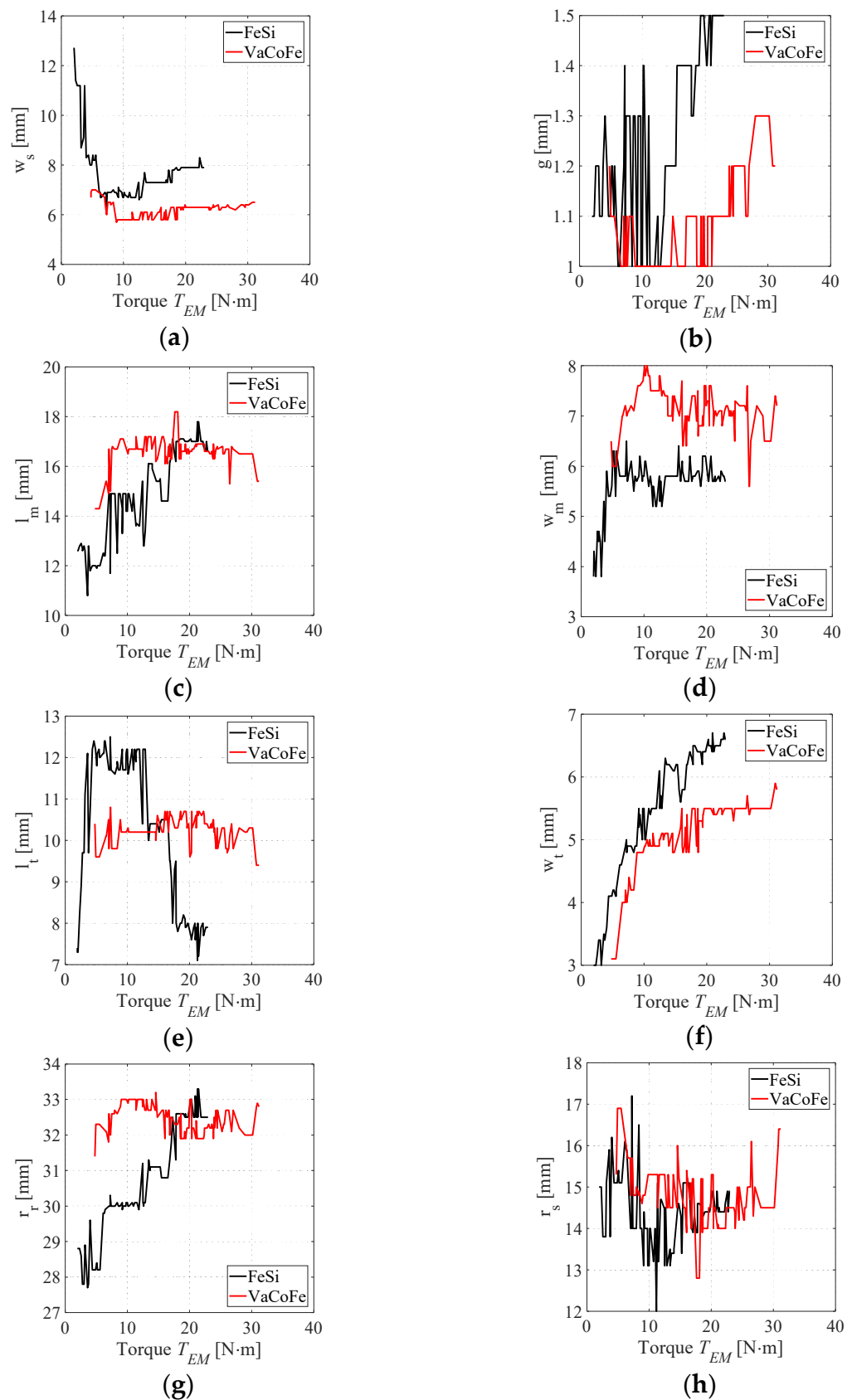


Figure 12. Decision variables for FeSi and VaCoFe core optimization sorted by increasing torque: (a) stator outer ring width w , (b) airgap size g , (c) magnet length l_m , and (d) width w_m , (e) stator teeth length l_t and (f) width w_t , (g) rotor radius r_r and (h) shaft radius r_s .

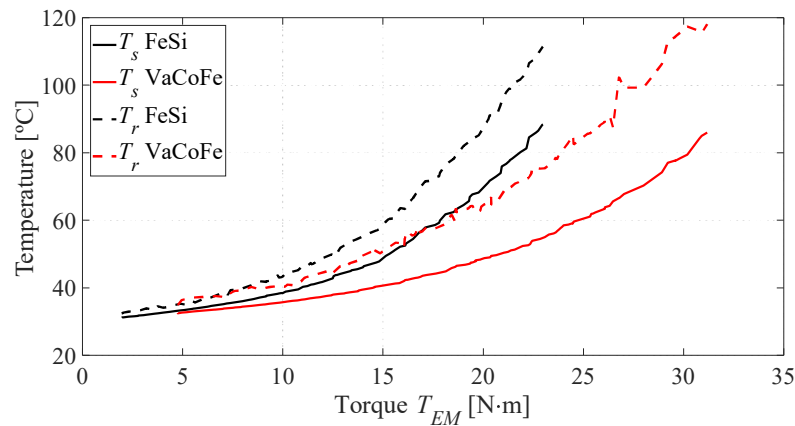


Figure 13. Surface and rotor temperatures of the last generation for FeSi and VaCoFe cores.

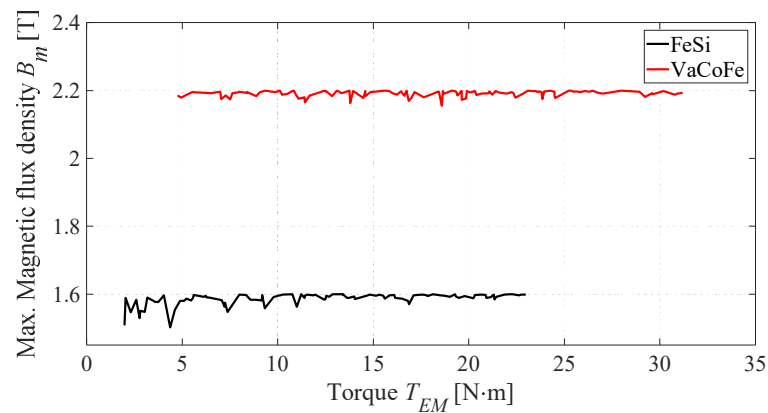


Figure 14. Maximum magnetic flux density of the last generation for FeSi and VaCoFe cores.

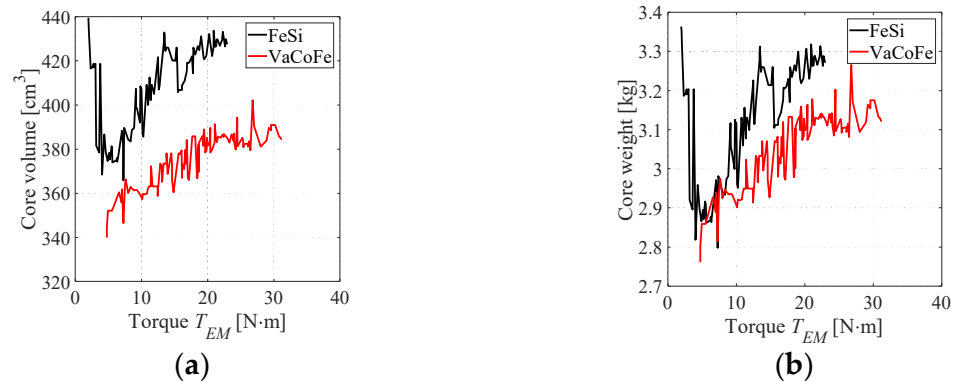


Figure 15. Core (a) volume and (b) weight of the last generation for FeSi and VaCoFe cores.

On the other hand, for the same available space, VaCoFe allowed reaching up to around 30 N·m, while FeSi resulted in 23 N·m with lower levels of efficiency. Further analysis is needed on the impact of these results on battery size and overall track performance to determine if the additional costs of manufacturing VaCoFe core motors are justified. These costs can be high, as the FeSi material for the prototype in [11] was acquired at EUR 237.4 /kg, while the VaCoFe laminations for the test circuit cost EUR 770.7 /kg (3.3 times higher cost than FeSi) and need additional heat treatment to achieve optimum magnetic properties.

6. Detailed Analysis of Selected Geometries

Three geometries were selected for further detailed analysis and validation of the optimization results: FeSi at 20 N·m (F20) and VaCoFe at 20 N·m (V20) and 30 N·m (V30),

corresponding to the Pareto front points presented in Figure 11b. These geometries are simulated with a rotating time-dependent 2D finite element model to obtain torque ripple and consider the effect of temporal and spatial flux density harmonics on core losses and overall efficiency. The selected optimized geometries are presented in Figure 16, and their dimensions in Table 3.

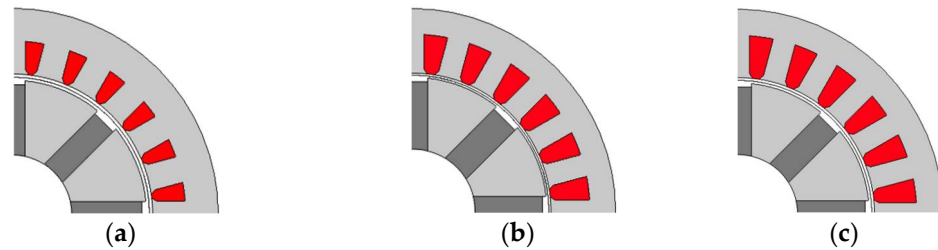


Figure 16. Selected optimized geometries: (a) F20, (b) V20, (c) V30.

Table 3. Decision variables of selected geometries.

Variable	F20	V20	V30
r_r	32.5 mm	33 mm	32 mm
w_s	7.9 mm	6.3 mm	6.4 mm
w_m	6.2 mm	7.3 mm	6.5 mm
l_m	17.0 mm	16.6 mm	16.5 mm
w_t	6.4 mm	5.5 mm	5.5 mm
l_t	8.0 mm	9.6 mm	10.3 mm
g	1.5 mm	1.0 mm	1.3 mm
r_s	14.4 mm	15.3 mm	14.5 mm
J_{oq}	48.2 A/mm ²	25.5 A/mm ²	42.0 A/mm ²
P_{PM}	17.57 W	18.66 W	39.27 W
P_{core}	65.1 W	62.41 W	64.66 W
P_{Cu}	875.5 W	391.4 W	1110 W
Efficiency	92.8%	96.4%	93.9%
Torque density	4.7 N·m/kg	4.7 N·m/kg	7.1 N·m/kg

It is noted that tooth lips were added to the stator teeth to consider a more realistic design than the simplified geometry considered for optimization. Between F20 and V20, the differences were mainly in the stator. The width of the magnetic circuit in F20 was wider to avoid core saturation as FeSi presents a lower saturation point than VaCoFe. V20 and V30 have similar dimensions, with the slot current density being the main difference. Current density is the main factor in increasing torque as the temperature is not a limitation at this point, whereas core dimensions are defined by the saturation constraint.

6.1. Core Losses

Because the airgap is not constant, discrete winding distribution and voltage/current time harmonics, the magnetic flux density waveform is not purely sinusoidal. Furthermore, in electrical machines, the magnetic fields are rotating, causing additional losses. To consider some of these effects, Equation (8) was adapted by assuming that the total core loss is the sum of losses for each harmonic.

An FEM time-dependent simulation was used to obtain magnetic flux waveforms in the machine. The average magnetic flux density in each element was estimated considering the model's shape functions. Core losses in each element were computed by summing the separate contribution of the harmonics of the radial and tangential components of the magnetic flux density, obtained from Fourier transformation Equation (26) [21].

$$p_i = \sum_n k_h f_n (B_{r_{n,i}}^2 + B_{\theta_{n,i}}^2) + k_e f_n^2 (B_{r_{n,i}}^2 + B_{\theta_{n,i}}^2) + k_{exc} f_n^{1.5} (B_{r_{n,i}}^{1.5} + B_{\theta_{n,i}}^{1.5}) \quad (26)$$

In (26), p_i is the core loss density in element i , f_n is the n^{th} frequency harmonic, and B_r and B_θ are the radial and tangential magnetic flux density components, respectively. k_h , k_e , and k_{exc} are the hysteresis, eddy current, and excess losses coefficients obtained from the material's specific losses curve. The steps to compute p_i for a specific element i are presented in Figure 17. The exemplified element is located near the tip of the stator tooth, Figure 17a. The magnetic flux density here is non-sinusoidal and presents a high tangential component as it is affected by the variation of reluctance from the non-uniform airgap during rotation, Figure 17b. As such, there is a relevant harmonic content that, from Equation (26), contributes to higher core loss density in elements near the airgap than in other parts of the machine where the flux density waveform is more sinusoidal.

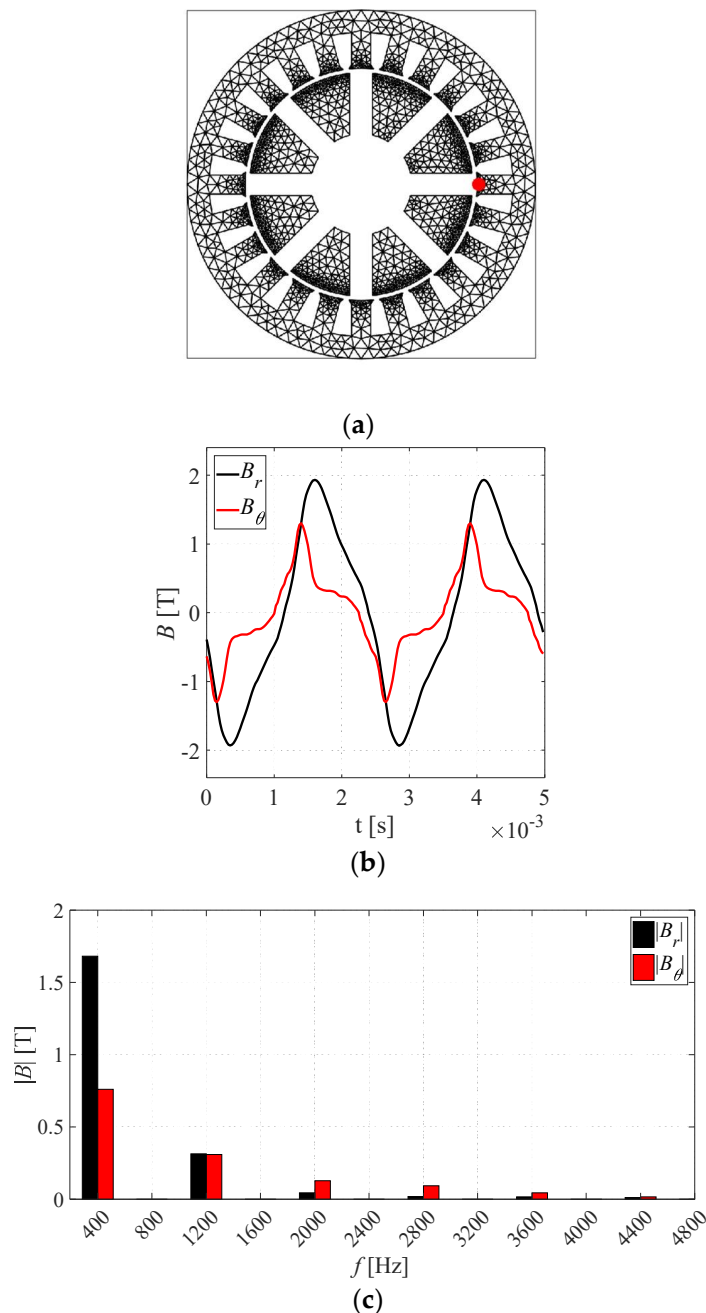


Figure 17. Steps for computation of losses density, example for element i (red dot). (a) Example of core geometry mesh, (b) waveform of flux density radial and tangential components in element i , (c) waveforms' Fourier transformation.

Because the flux distribution is computed from the 2D simulation, it is assumed that the flux distribution is the same along the length, L , of the machine. Total core losses, P_{core} , are obtained from the sum of the losses in each element, i , density ρ , and area A_i , Equation (27).

$$P_{core} = \sum_i \rho A_i L \cdot p_i \quad (27)$$

In conductive materials with induced currents, such as permanent magnets and shaft, Joule losses are computed from Equation (28), where V is the PMs volume, σ the conductivity, and \mathbf{J} the PMs induced current density variation in time.

$$P_{PM} = \int_V \frac{|\mathbf{J}|^2}{\sigma} dV \quad (28)$$

The efficiency was computed considering winding losses, as in the previous section, and core and induced current losses with these presented methods.

6.2. Results

The selected geometries were simulated with a 2D time-dependent simulation for the optimized load angle ($i_d = 0$ and $i_q = I_m$) at a nominal electrical frequency of 400 Hz. The magnetic flux density distribution was, as expected, with the flux density norm in the stator teeth around the set maximum for optimization (1.6 T for FeSi and 2.2 T), Figure 18. The slight differences between optimization results and simulation are due to the changes made to the simplified geometry.

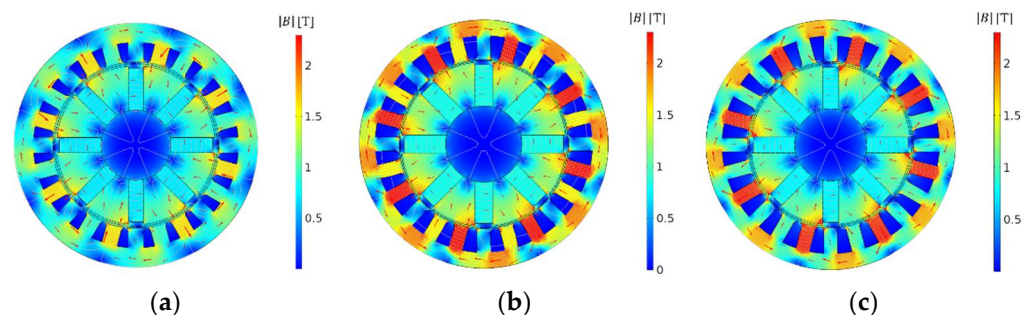


Figure 18. Distribution of magnetic flux distribution of selected geometries (a) F20, (b) V20, and (c) V30.

The instantaneous torque in time is presented in Figure 19 for the selected geometries. The spoke-type IPMSM results in a relatively higher torque ripple than other topologies due to the flux concentration in the airgap [25]. VaCoFe's higher saturation point allows higher flux concentration in the airgap and, consequently, V20 and V30 presented higher torque ripple than F20. V20 presented a peak-to-peak ripple of 7 N·m, V30 of 5.6 N·m, and F20 of 2.1 N·m. However, the ripple could be reduced while approximately maintaining the average torque with further analysis focused on dimensioning a non-uniform airgap that distributes the flux in the airgap more evenly through shaping the rotor poles and/or stator teeth [25]. Preliminary results of these adjustments are shown further.

The average torque values predicted with the 2D stationary (2D static) model used for optimization, based on stationary simulations, were in accordance with the results obtained from the 2D time-dependent (2D-time) simulation with a maximum deviation of 2.28% for the V20 geometry, as presented in Table 4. This low deviation was mainly due to the parameterization of the d - q model with 2D FE simulation, which considers the nonlinearity of the magnetic circuit and saturation of the material. Nonetheless, the model does not consider ripple and harmonics, so some deviations were expected.

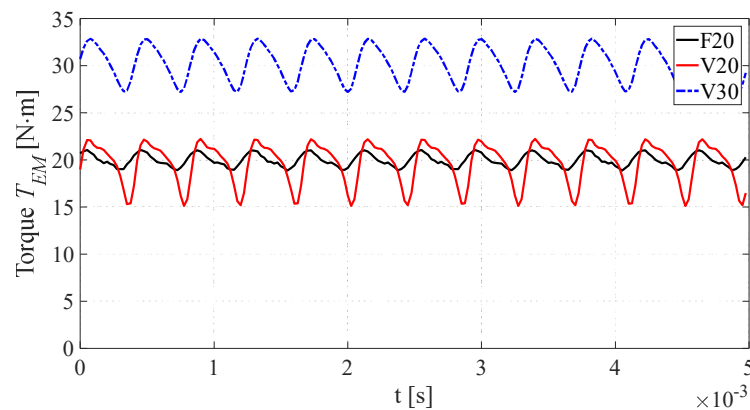


Figure 19. Instantaneous torque considering $i_d = 0$ of selected geometries: F20, V20, and V30.

Table 4. Average torque and efficiency obtained from 2D stationary model and 2D time-dependent model.

	Avg. Torque [N·m]		Efficiency [%]	
	2D-Time	2D-Static	2D-Time	2D-Static
F20	19.95	19.78 (−0.84%)	93.11	92.84 (−0.27%)
V20	19.62	20.07 (+2.28%)	96.31	96.39 (+0.08%)
V30	30.31	29.81 (−1.64%)	94.21	93.92 (−0.29%)

In terms of efficiency, there was a maximum difference of 0.29% for the V30 geometry. The accuracy of the efficiency depends mostly on the estimation of losses, as output power is similar. Figure 20 presents the separation of the losses computed with time-dependent FE simulation and the stationary model used for optimization based on stationary FE simulations for the chosen geometries. Because copper losses account for most of the total losses of the motor, and these are computed the same way in both models, both give similar values of efficiency. It is noted that the skin effect can cause additional losses limiting the maximum slot windings' wire gauge to a 2.8 mm radius (skin depth at 533 Hz/8000 rpm). This was achieved with multi-strand wires with a thickness of less than 1 mm, with multiple conductors in parallel as conducted in the previous FeSi IPMSM [11]. Despite the simplifications made for the computation of permanent magnet and core losses, considering only the magnetic flux's fundamental component done in the optimization model, the results seem to be a close overestimation of the ones obtained using the FE time-dependent model. For both models, the iron losses give similar results, with slightly higher values obtained with time-dependent FE simulation, because of the additional effects considered in computing them. The overestimation was due to differences in the estimation of losses in the permanent magnet and shaft. This is because, in the optimization model, the whole magnet volume was considered to be affected by the same magnetic flux variation. On the other hand, with time-dependent FE simulation, the non-uniform distribution of induced currents was captured, and losses were produced only in regions closer to the airgap.

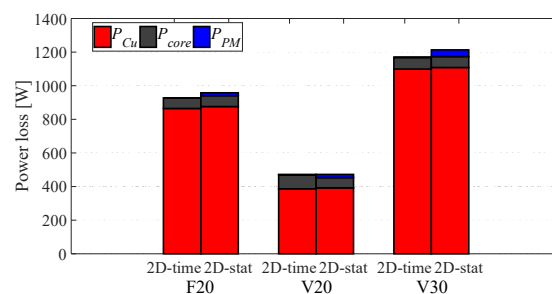


Figure 20. Losses computed using 2D time-dependent FE simulation (2D-time) and the 2D stationary model used for optimization (2D-static) for the chosen geometries.

In addition, the higher torque ripple of the V20 and V30 topologies could also be reduced with changes to the shape of the rotor by, for example, adding protrusions around the magnets, as seen in Figure 21. This resulted in a more even flux distribution in the airgap, reducing ripple and approximately maintaining the average torque. Using this geometry, V20 and V30 presented similar average torques of 20.78 N·m and 29.92 N·m, respectively. The peak-peak torque ripple was reduced from 7.0 N·m to 4.3 N·m for the new V20 and from 5.6 N·m to 4.6 N·m for the new V30, Table 5. These results were obtained using a 2D-time-dependent simulation. Additional torque ripple attenuation could be achieved by also adjusting the curvature shape of the rotor poles or the stator tooth lips, which will be further analyzed for the final construction of the prototypes.

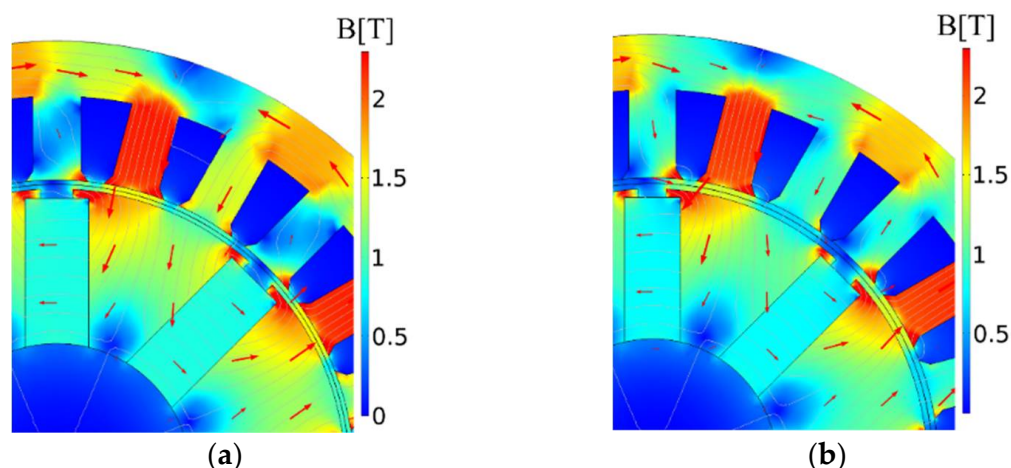


Figure 21. Magnetic flux distribution of geometries with changed rotor shape of (a) V20, new and (b) V30, new.

Table 5. Average torque and torque ripple.

Geometry	Avg. Torque [N·m]	Peak-Peak Torque Ripple [N·m]
V20	19.62	7.0
V20—new	20.78	4.3
V30	30.31	5.6
V30—new	29.92	4.6

The flux density distribution in the permanent magnets was also analyzed at maximum torque and maximum direct current ($i_d = I_m$) conditions. For the three presented geometries, the simulation did not suggest considerable demagnetization, with flux density levels above the knee-point (0.4 T for the N40H magnets at worst-case 120 °C), in most of the magnets, for both cases. At the nominal operating point, because the machine geometries were optimized for maximum torque at $i_d = 0$, the resulting power factor is high for all geometries being 0.990 for F20, 0.994 for V20, and 0.980 for V30.

7. Conclusions

A spoke-type IPMSM geometry was optimized considering FeSi and VaCoFe cores for a range of torque/efficiency to provide a general comparative analysis between materials. This is particularized for a four-motor competition vehicle's powertrain. A genetic optimization algorithm (NSGA-II) is applied over a hybrid analytical/finite-element model of the motor to provide sufficiently accurate electromagnetic and thermal results within a feasible time. The characterization of the materials for the optimization model is based on each's magnetic properties; in particular, the VaCoFe B - H curve was obtained experimentally and presented.

According to the presented model, it is shown that the VaCoFe core results in a better machine across both torque and efficiency ranges. VaCoFe can result in an estimated

increase of up to 5% in efficiency for the same torque or up to 64% torque increase for the same efficiency level. For the same available space, the VaCoFe can reach up to around 30 N·m, while the FeSi only 23 N·m with lower levels of efficiency.

These results are dependent on the accuracy of the presented 2D-static model, where only the magnetic flux's fundamental component is considered in the computation of permanent magnet and core losses. Moreover, because VaCoFe can cost around 3.3 times more than FeSi, more than usual attention to simulation accuracy is necessary before investing and building a final prototype. A more accurate time-dependent 2D simulation was used to evaluate the three chosen geometry designs, and a method was implemented to compute discriminated losses in the windings, PMs, and core material. Two geometries of VaCoFe and FeSi with 20 N·m, the target torque of the in-wheel motors for the competition vehicle, and a VaCoFe at 30 N·m, around the maximum torque motor obtained through optimization, were analyzed.

It is shown that the analytical/finite-element model used for optimization, based on stationary simulations of a quarter of the machine's magnetic circuit, gives results in accordance with the commonly more accurate time-dependent simulation, with deviations lower than 2.28% for the average torque and 0.29% in efficiency, with less computational cost, for the studied operation point. As such, it might be used for similarly computationally-intensive studies, as a first approach, to machine design as a quicker and almost as accurate alternative to FE model-based approaches.

Comparing the selected geometries, the torque ripple is higher for the VaCoFe designs than the FeSi one, mainly because of the higher flux density in the airgap. However, this can be attenuated by adjusting the shape of the rotor poles through further optimizations of the obtained designs with this objective. Overall, further analysis is needed using a more complete 3D model for the machine to study additional effects (e.g., border effects) not accounted for in 2D models.

The presented analysis is promising for building final prototypes and provides a comparative analysis of the possible advantages of using VaCoFe as an alternative core material to traditional FeSi for high specific-torque electric vehicles and aircraft applications. The authors are now working on the construction of the optimized geometry of the VaCoFe machine.

Author Contributions: Conceptualization, methodology, P.P.C.B. and J.F.P.F.; validation, P.P.C.B. and J.F.P.F.; formal analysis, investigation, P.P.C.B.; resources, J.F.P.F. and P.J.C.B.; writing—original draft preparation, writing—review and editing, P.P.C.B., L.F.D.B., J.F.P.F. and P.J.C.B.; supervision, J.F.P.F. and P.J.C.B. All authors have read and agreed to the published version of the manuscript.

Funding: This work is financed by national funds through FCT—Foundation for Science and Technology, I.P., through IDMEC, under LAETA, project UIDB/50022/2020.

Institutional Review Board Statement: Not applicable.

Informed Consent Statement: Not applicable.

Data Availability Statement: Not applicable.

Conflicts of Interest: The authors declare no conflict of interest.

References

1. NASA Aeronautics. *NASA Aeronautics: Strategic Implementation Plan: 2019 Update*; Technical Report NP-2017-01-2352-HQ; National Aeronautics and Space Administration (NASA): Washington, DC, USA, 2019.
2. Jayaraman, T. Effect of Processing of HIPERCO[®] 50 Alloy Laminates on Their Magnetic Properties. *J. Electron. Mater.* **2005**, *44*, 4379–4386. [[CrossRef](#)]
3. Krings, A.; Cossale, M.; Tenconi, A.; Soulard, J.; Cavagnino, A.; Boglietti, A. Magnetic materials used in electrical machines: A comparison and selection guide for early machine design. *IEEE Ind. Appl. Mag.* **2017**, *23*, 21–28. [[CrossRef](#)]
4. Zhang, X.; Haran, K.S. High-specific-power electric machines for electrified transportation applications-technology options. In Proceedings of the 2016 IEEE Energy Conversion Congress and Exposition (ECCE), Milwaukee, WI, USA, 18–22 September 2016.

5. Palmieri, M.; Perta, M.; Cupertino, F. Design of a 50.000-r/min Synchronous Reluctance Machine for an Aeronautic Diesel Engine Compressor. *IEEE Trans. Ind. Appl.* **2016**, *52*, 3831–3838. [[CrossRef](#)]
6. Fernando, N.; Vakil, G.; Arumugam, P.; Amankwah, E.; Gerada, C.; Bozhko, S. Impact of Soft Magnetic Material on Design of High-Speed Permanent-Magnet Machines. *IEEE Trans. Ind. Electron.* **2017**, *64*, 2415–2423. [[CrossRef](#)]
7. Mecrow, B.C.; Jack, A.G.; Atkinson, D.J.; Green, S.R.; Atkinson, G.J.; King, A.; Green, B. Design and testing of a four-phase fault-tolerant permanent-magnet machine for an engine fuel pump. *IEEE Trans. Energy Convers.* **2004**, *19*, 671–678. [[CrossRef](#)]
8. Krings, A.; Boglietti, A.; Cavagnino, A.; Sprague, S. Soft Magnetic Material Status and Trends in Electric Machines. *IEEE Trans. Ind. Electron.* **2017**, *64*, 2405–2414. [[CrossRef](#)]
9. Volbers, N.; Gerster, J. High Saturation, High Strength Iron-Cobalt Alloy for Electrical Machines. *Proc. INDUCTICA CWIEME Berl.* **2012**, 1–4.
10. Zhang, X.; Bowman, C.L.; O’Connell, T.; Haran, K.S. Large electric machines for aircraft electric propulsion. *IET Electr. Power Appl.* **2018**, *12*, 767–779. [[CrossRef](#)]
11. Bhagubai, P.; Sarrico, J.; Fernandes, J.; Branco, P. Design, Multi-Objective Optimization, and Prototyping of a 20 kW 8000 rpm Permanent Magnet Synchronous Motor for a Competition Electric Vehicle. *Energies* **2020**, *13*, 2465. [[CrossRef](#)]
12. Deb, K.; Pratap, A.; Agarwal, S.; Meyarivan, T. A Fast Elitist Multiobjective Genetic Algorithm NSGA-II. *IEEE Trans. J. Evol. Comput.* **2002**, *6*, 182–197. [[CrossRef](#)]
13. Han, W.; Van Dang, C.; Kim, J.; Kim, Y.; Jung, S. Global-Simplex Optimization Algorithm Applied to FEM-Based Optimal Design of Electric Machine. *IEEE Trans. Magn.* **2017**, *53*, 1–4. [[CrossRef](#)]
14. Bianchi, N.; Bolognani, S.D. Design Optimisation of Electric Motors by Genetic Algorithms. *IEE Proc. Electr. Power Appl.* **1998**, *145*, 475–483. [[CrossRef](#)]
15. Fatemi, A.; Ionel, D.M.; Popescu, M.; Chong, Y.C.; Demerdash, N.A.O. Design Optimization of a High Torque Density Spoke-Type PM Motor for a Formula E Race Drive Cycle. *IEEE Trans. Ind. Appl.* **2018**, *54*, 4343–4354. [[CrossRef](#)]
16. Kesgin, M.G.; Han, P.; Taran, N.; Ionel, D.M. Optimal Study of a High Specific Torque Vernier-type Axial-flux PM Machine with Two Different Stators and a Single Winding. In Proceedings of the 2020 IEEE Energy Conversion Congress and Exposition (ECCE), Detroit, MI, USA, 11–15 October 2020.
17. Fatemi, A.; Ionel, D.M.; Demerdash, N.A.O.; Nehl, T.W. Optimal Design of IPM Motors With Different Cooling Systems and Winding Configurations. *IEEE Trans. Ind. Appl.* **2016**, *52*, 3041–3049. [[CrossRef](#)]
18. Bhagubai, P.P.C.; Cardoso, A.C.; Fernandes, J.F.P. Cobalt Iron Core Impact on Optimal Design of an Interior Permanent Magnet Synchronous Motor for Competition Electric Vehicle. In Proceedings of the 2020 2nd Global Power, Energy and Communication Conference (GPECOM), Izmir, Turkey, 20–23 October 2020.
19. Gmyrek, Z.; Cavagnino, A.; Vaschetto, S.; Bramerdorfer, G. Loss Modeling for Interlocked Magnetic Cores. In Proceedings of the 2020 IEEE Energy Conversion Congress and Exposition (ECCE), Detroit, MI, USA, 11–15 October 2020; pp. 1060–1066.
20. Lee, J.-Y.; Lee, S.-H.; Lee, G.-H.; Hong, J.-P.; Hur, J. Determination of Parameters Considering Magnetic Nonlinearity in an Interior Permanent Magnet Synchronous Motor. *IEEE Trans. Magn.* **2006**, *42*, 1303–1306.
21. Yamazaki, K.; Seto, Y. Iron loss analysis of interior permanent-magnet synchronous motors-variation of main loss factors due to driving condition. *IEEE Trans. Ind. Appl.* **2006**, *42*, 1045–1052. [[CrossRef](#)]
22. Yamazaki, K.; Fukuoka, T.; Akatsu, K.; Nakao, N.; Ruderman, A. Investigation of Locked Rotor Test for Estimation of Magnet PWM Carrier Eddy Current Loss in Synchronous Machines. *IEEE Trans. Magn.* **2012**, *48*, 3327–3330. [[CrossRef](#)]
23. Huang, W.; Bettayeb, A.; Kaczmarek, R.; Vannier, J. Optimization of Magnet Segmentation for Reduction of Eddy-Current Losses in Permanent Magnet Synchronous Machine. *IEEE Trans. Energy Convers.* **2010**, *25*, 381–387. [[CrossRef](#)]
24. Fénot, M.; Bertin, Y.; Dorignac, E.; Lalizel, G. A Review of Heat Transfer between Concentric Rotating Cylinders with or without Axial Flow. *Int. J. Therm. Sci.* **2011**, *50*, 1138–1155. [[CrossRef](#)]
25. Hwang, K.Y.; Jo, J.H.; Kwon, B.I. A Study on Optimal Pole Design of Spoke-Type IPMSM With Concentrated Winding for Reducing the Torque Ripple by Experiment Design Method. *IEEE Trans. Magn.* **2009**, *45*, 4712–4715. [[CrossRef](#)]